DOI: 10.19884/j.1672-5220.202402002

Generation and Expulsion of Gas Rings within Liquid Film in Agitated Thin-Film Evaporator

CHAI Jin, HUANG Yao*, PENG Yitian, ZOU Kun
College of Mechanical Engineering, Donghua University, Shanghai 201620, China

Abstract: The agitated thin-film evaporator (ATFE) plays a crucial role in evaporation and concentration processes. The design of the scraper for processing high-viscosity non-Newtonian fluids in the ATFE is complex. The intricate scraping action of the scraper introduces gas into the liquid film, leading to the formation of a gas ring along the wall. This process subsequently reduces wall heat flow, thereby affecting heat transfer. Computational fluid dynamics (CFD) is used to simulate the flow field of the non-Newtonian fluid in the ATFE. The investigation focuses on understanding the mechanism behind the formation of gas rings in the liquid film and proposes methods to prevent their formation. The results demonstrate a transition of the gas from a gas ring suspended in the liquid to a gas ring attached to the wall after entering the liquid film. The scraping action around the circumference of the scraper helps to expel gas rings, indicating the necessity of adjusting the scraper arrangement and increasing the frequency of scraping to enhance gas ring expulsion. The spiral motion of the bow wave serves as the source of gas entry into the liquid film. Therefore, the rotation speed can appropriately increase to reduce the size of the bow wave, thereby inhibiting the formation of the gas ring from the source. This research investigates the mechanism of gas ring generation and expulsion, offering theoretical guidance for processing high-viscosity non-Newtonian materials in the flow field of the ATFE.

Keywords: agitated thin-film evaporator (ATFE); non-Newtonian fluid; gas ring; high viscosity
CLC number: TH49 **Document code**: A
Article ID: 1672-5220(2025)01-0041-13

Open Science Identity (OSID)

0 Introduction

As a novel type of evaporation equipment, the agitated thin-film evaporator (ATFE)[1] offers advantages such as high evaporation efficiency, compact sizes, high product quality, wide applicability, and easy maintenance and cleaning. It demonstrates a commendable evaporation and concentration effect on both low-viscosity and high-viscosity materials. Following the introduction of the ATFE in the 1940s[2], numerous domestic and international researchers have extensively studied its internal mixing and heat transfer processes. They have proposed various models related to fluid, heat and mass transfer. Initially, Mutzenburg[3] segmented the flow field of the ATFE into three components: the film area, the bow wave and the drag-flow. McKelvey et al.[4] hypothesized that the film formed by the fluid within the stirring apparatus remained stationary under conditions of high fluid viscosity. The key to understanding overall fluid transport lies in comprehending the flow that occurs in the bow wave. Komori et al.[5] experimentally found that 70%–90% of the fluid spiraled downward in the bow wave, and the liquid film could be considered to exhibit the laminar flow. Kern et al.[6] argued that heat transfer occurred through the thermal conductivity of the liquid film. Kool[7] concluded that the heat transfer rate depended on the thermal conductivity rate, and increased rapidly when the liquid layer was continuously renewed. They also found that the heat transfer coefficient was a function of fluid physical properties, rotation speeds and the number of scrapers.

It is worth noting that bubbles formed in the evaporation field near the heated wall surface can affect the evaporation efficiency. Abdoulaye et al.[8] found that 1 ms to 2 ms after bubble generation, bubbles in the inertia-controlled growth period took the form of hemispheres covering the surface of the heater, forming wall bubbles. During this period, the heat flow of the liquid decreased. Wei et al.[9] used the volume of fraction (VOF) model to simulate the evaporation of water in a medium subjected to single-wall heating in a rectangular channel. The researchers

Received date: 2024-02-04
Foundation items: National Natural Science Foundation of China (No. 51905089); Fundamental Research Funds for the Central Universities, China (No. 2232020D-31)
* Correspondence should be addressed to HUANG Yao, email: huanghuang36@dhu.edu.cn
Citation: CHAI J, HUANG Y, PENG Y T, et al. Generation and expulsion of gas rings within liquid film in agitated thin-film evaporator[J]. *Journal of Donghua University (English Edition)*, 2025, 42(1): 41-53.

observed that many bubbles merged to form larger bubbles. Moreover, the diameter and the growth rate of wall bubbles increased as the heat flux rose. Fan et al.[10] used a two-dimensional model to simulate the formation of bubbles on the wall surface during descending film evaporation. The researchers concluded that bubbles detached from the surface due to the shear force as they increased in size within a liquid film. This generation and the detachment of bubbles could enhance the heat transfer.

During the processing of non-Newtonian fluids, the ATFE typically develops gas rings on their walls, and the excessive accumulation of gas at these walls[11] leads to a decrease in the heat transfer coefficient, which affects the efficiency of evaporation. Previous studies have investigated the mechanism of bubble generation and its impact on heat transfer in the field of evaporation from various perspectives, including theory and experimentation. Nonetheless, few research has studied the impact of scraper scraping on the formation of gas rings in the flow field. The scraper forms of the ATFE are categorized as in-line and sawtooth. The in-line scraper can efficiently handle low-viscosity non-Newtonian fluids, but the uniformity and the continuity of the liquid film deteriorate when dealing with non-Newtonian fluids with high zero-shear viscosity. The special characteristics of high-viscosity non-Newtonian fluids[12] make the design of the scraper very complex. As a result of the complex scraping action of the scraper, gas can easily become trapped in the liquid film, forming a gas ring inside the liquid film. Hann et al.[13] experimentally investigated and visually observed the process of bubble generation and annihilation when air sheared a water stream. The above experiments were conducted using non-Newtonian fluids by a scraper in the ATFE under the above-mentioned experimental conditions, and bubbles were introduced during the scraper agitation. Zenit et al.[14] experimentally found that bubbles dispersed without significant aggregation in Newtonian fluids, whereas they tended to form vertical bimodal peaks and large aggregates when moving in non-Newtonian fluids. Ohta et al.[15] conducted numerical simulations to examine the shear flow field of liquid bubbles moving in non-Newtonian fluids like carboxymethyl cellulose (CMC). They discovered a significant reduction in the viscosity around the bubbles, with the most pronounced decrease in the viscosity near the bubbles. During the operation of the ATFE, gas could become trapped in the liquid film or even form a gas ring attached to the wall. However, many studies have not addressed the reasons for the formation of the wall-attached gas ring in the flow field of the ATFE, nor have they proposed methods to resolve this issue. Hence, it is essential to examine the distribution of the flow field in the ATFE, investigate the mechanism of gas ring formation and prevent the formation of the wall-attached gas ring.

This paper investigates the process of gas ring generation and expulsion based on the VOF three-dimensional two-phase flow model. The aim is to offer a theoretical direction in diminishing wall-attached gas rings within the flow field of the ATFE.

1 Model Building

1.1 Physical modeling

To investigate the gas ring within the liquid film, this study employs a simplified ATFE model and conducts numerical simulations using the Fluent software. The ATFE is a hollow cylinder with an outer diameter of 250 mm and a height of 150 mm, with the scraper tip maintaining at 1 mm from the wall, as shown in Fig. 1. This setup is like that in Refs. [5, 16]. The quarter model is consistently used for this paper and a mesh with a periodic grid is employed. To obtain a clearer view of the liquid film development on the wall and the shape of the bow wave, the surface mesh is refined both on the wall and at the inlet. The mesh has a fixed dimension of 0.25 mm, with a growth rate of 1.15, a minimum mesh size of 0.25 mm and a maximum mesh size of 2.50 mm for the remaining surface mesh, and a quarter-periodic boundary is established. To improve the computational accuracy in the field of the computational analysis, a tetrahedral mesh is utilized for the body mesh. The total surface mesh count is 1 120 000, with a peak skewness of 0.73. The body mesh totals 10 710 000, and the mesh quality is 0.85. As shown in Fig. 1, the moments of the rotor are depicted under different counts of grid elements. As verified by the grid independence, the moment remains essentially constant when the count of grid elements is greater than 10^7.

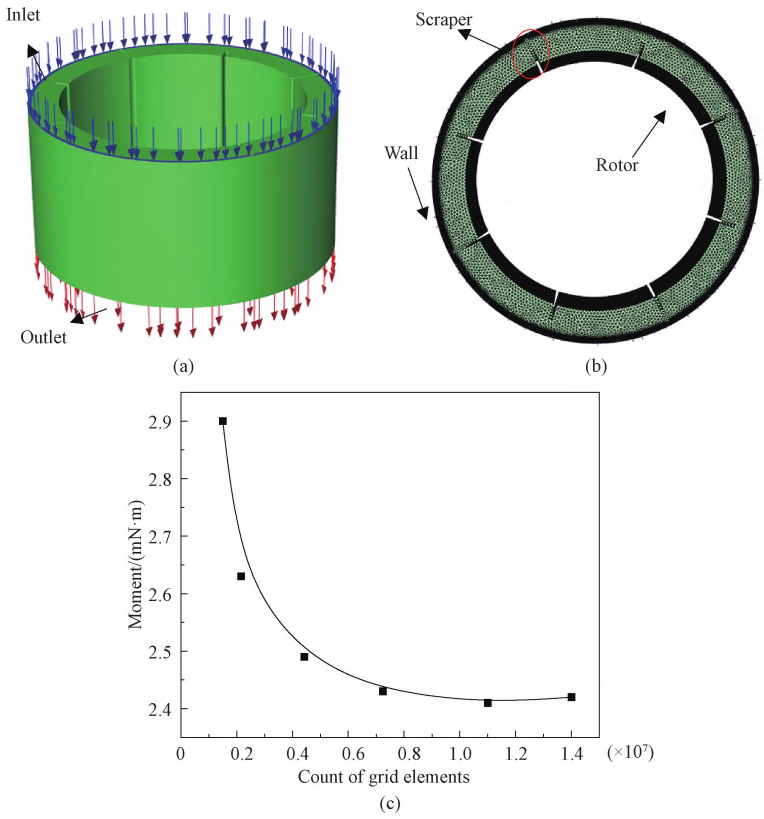

Fig. 1 Schematic diagram of ATFE structure: (a) structure diagram; (b) meshing diagram; (c) moments with different counts of grid elements

1.2 Configuration of control equations and solutions

The VOF method[17] is used to solve pressure and velocity variations of the two-phase flow of incompressible Newtonian fluids by coupling the continuity equation and the Navier-Stokes equation. The volume of fluid functions method derived from the Fluent software is used to monitor the two-phase gas-liquid interface. The equations for the mass conservation and the momentum conservation are

$$\nabla \cdot \boldsymbol{u} = 0, \tag{1}$$

$$\frac{\partial(\rho \boldsymbol{u})}{\partial t} + \nabla \cdot (\rho \boldsymbol{u}\boldsymbol{u}) = -\nabla p + \rho g + \nabla \cdot (\mu(\nabla \boldsymbol{u} + \nabla^{\mathrm{T}} \boldsymbol{u})) + \boldsymbol{f}_{\sigma v}, \tag{2}$$

where ∇ is the Laplace operator; $\boldsymbol{u}$ is the velocity vector; p is the pressure; g is the gravitational acceleration; $\boldsymbol{f}_{\sigma v}$ is several interfacial forces acting on the interface; μ and ρ are the viscosity of the fluid and the density of the fluid, respectively.

The density and the viscosity of the control body in the VOF model are[18]

$$\rho = \alpha\rho_1 + (1-\alpha)\rho_2, \tag{3}$$

$$\mu = \alpha\mu_1 + (1-\alpha)\mu_2, \tag{4}$$

where α in the VOF model represents the volume fraction of the two different fluids and varies smoothly between 0 and 1; ρ_1 and ρ_2 refer to the densities of the two different fluids; μ_1 and μ_2 refer to the viscosities of the two different fluids.

In this study, the selected simulation framework is an integrated pressure-velocity algorithm which is founded on a pressure solver. A single reference system (SRF) is selected to achieve the scraper rotational movement and ensure the material consistent entry at a mass flow rate of 0.1 m/s. Subsequently, the material is introduced into the scraper at a mass flow rate of 0.1 m/s. For ease of computation, this paper presupposes the fluid continuity and incompressibility. Based on the properties of the ATFE flow field, the k-ω turbulence model is used to characterize intense turbulence at the wall and precisely mimic the flow close to the wall.

The k-ω turbulence model[19], an enhanced variant of the k-ε turbulence model, effectively replicates boundary flow and delivers precise turbulence boundary conditions.

1.3 Simulation media

The ATFE is highly efficient in managing non-Newtonian fluids across a broad spectrum of viscosities. CMC[20] is a cellulose derivative. When the volume fraction of the CMC solution is between 1% and 3%, it does not exhibit the shear-thinning behavior. When the volume fraction of the CMC solution is above 4%, it usually exhibits the shear-thinning behavior. The rheological characteristics of CMC are expressed through a power-law model. The power-law fluid is a type of

non-Newtonian fluid, and the governing equation for its viscosity is related to the shear rate:

$$\mu = ks^{n-1}, \tag{5}$$

where k stands for the coefficient of consistency; s refers to the shear rate; n is the flow characteristic.

Power-law fluids[21] can be classified by the flow characteristic n: shear-thinning fluids ($n<1$), Newtonian fluids ($n=1$), and shear-thickening fluids ($n>1$).

Parameters for CMC are listed in Table 1[22], where μ_0 is the zero-shear-rate viscosity; μ_∞ is the infinite-shear-rate viscosity.

Table 1 Parameters for CMC

Parameter	Viscosity model	k	n	μ_0/(Pa·s)	μ_∞/(Pa·s)
Value	Power law model	4.44	0.48	4.50	0.01

2 Results and Discussion

2.1 Flow field distribution

In the ATFE, the gas easily becomes entrained in the liquid film due to the scraping of the scraper and the disturbing effects of the scraper. This paper focuses on the simplified model of the ATFE and investigates the mechanism of gas ring generation based on the established model. Figure 2 illustrates the flow field distribution of CMC in the ATFE, where red represents the material and blue represents the gas. The liquid film area ratio on the wall is defined as the ratio of the material area on the wall to the total wall area. Upon examining the wall phase diagram of the sawtooth scraper in Fig. 2, it is evident that the liquid film deposited on the wall by the grooved scraper is discontinuous. Approximately 90% of the wall surface is covered by the liquid film, while the remaining 10% is in the gas phase. Upon examining the flow field distribution in Fig. 2, it is evident that due to the circumferential scraping of the sawtooth scraper, some of the material can effectively pass through the gap between the tip of the scraper and the wall and create a liquid film on the inner wall surface of the evaporator. The remaining solution forms a bow wave at the leading edge of the scraper. The sawtooth scraper features a groove. When the bow wave encounters the groove during the spiral downward transport, it flows out from the groove and spreads in the circumferential direction on the liquid film. This outflow is referred to as the drag-flow. From the semi-transparent flow field diagram in Fig. 2, the presence of gas in the flow field is observed and sandwiched between the drag-flow and the liquid film. The gas which is distributed in an annular shape along the circumference is referred to as gas rings.

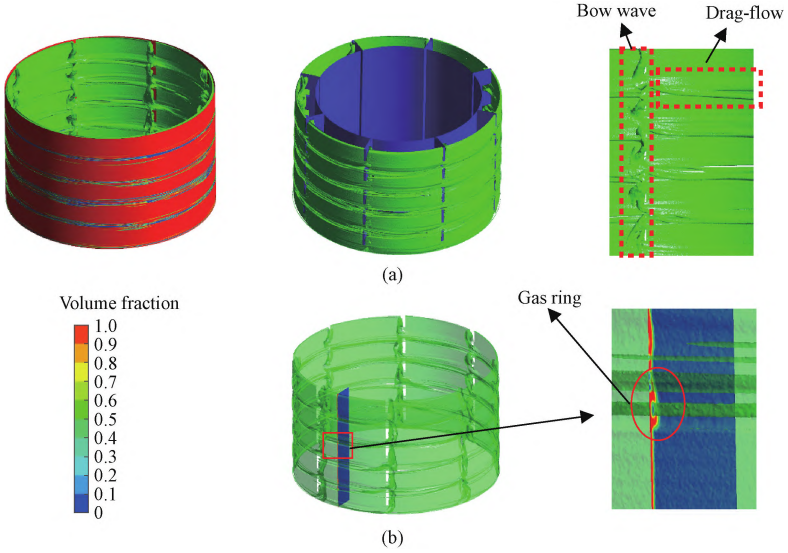

Fig. 2 Flow field distribution of CMC in ATFE: (a) structure of flow field; (b) gas ring in flow field

As shown in Fig. 3, the model is quarter-periodic. The average values are all extracted from the circumferential angle range from 0° to 90.0° and the axial height is 60 mm in the middle of the model. Firstly, the above data are divided into numerous intervals in the circumferential direction. Then, the average value within each interval is computed. Finally, a graph is created to depict the relationship between the circumferential angle and the average value. As shown in Fig. 4, the viscosity and the shear rate of the sawtooth scraper are described at the same operating conditions. From Fig. 4(a), when the scraper position is at 37.0°, the maximum viscosity at the scraper is around 1.6 Pa·s and the shear rate is around 160 s^{-1}. When the scraper position is at 23.0°, the lowest

viscosity at the scraper tip is only about 0.2 Pa · s, and the maximum shear rate is higher than 1 250 s^{-1}. It can be seen from Fig. 4(b) that the shear rate is maximum near the tip of the scraper and at the position where the drag-flow flows through, which is red. In the axial viscosity, the grey part is the notch position, the white part is the scraper position, the inlet is at 75 mm horizontal coordinate and the outlet is at −75 mm axis distance. At the inlet, the viscosity near the scraper is the largest, about 1.5 Pa · s. When being away from the inlet, the material cannot recover to the original viscosity. At an axial position of −58 mm, the peak axial viscosity at the sawtooth of the sawtooth scraper is eventually higher than 0.6 Pa · s; at an axial position of −70 mm, the valley axial viscosity at the groove of the sawtooth scraper is about 0.2 Pa · s. This is because when the material flows out from the groove, the outflow of the material forms the drag-flow. Relative motion occurs between the drag-flow and the liquid film, and the velocity gradient between the two is large. The shear rate at the groove is higher than that at the scraper, and the shear-thinning effect is enhanced. This is the reason why many large-capacity film evaporators have complex scraper designs.

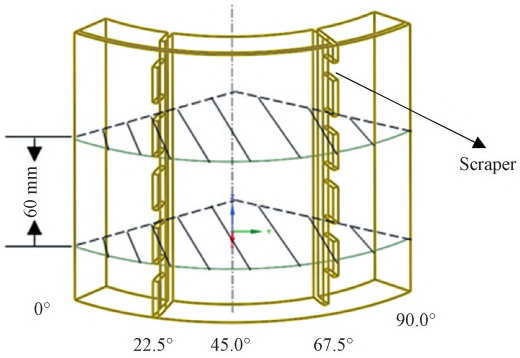

Fig. 3 Circumferential angle schematic diagram

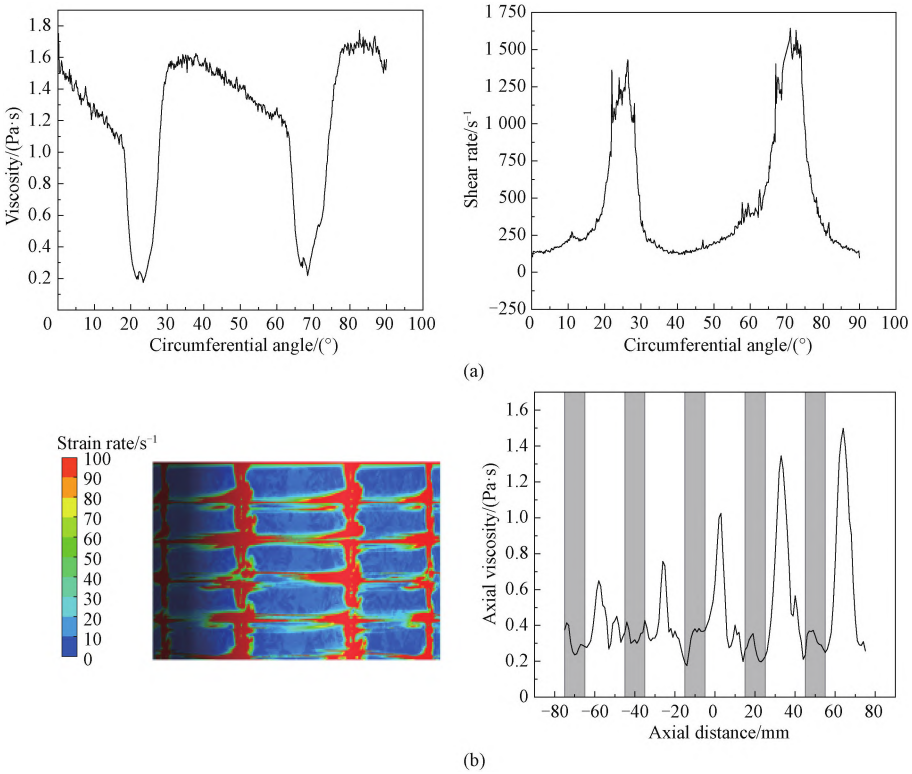

Fig. 4 Viscosity and shear rate of sawtooth scraper in ATFE: (a) viscosity and shear rate; (b) shear rate contour and axial viscosity

2.2 Mechanism analysis of gas rings within liquid film

2.2.1 Gas rings within liquid film

Due to the special characteristics of high-viscosity non-Newtonian fluids, the scraper design of the large-capacity thin-film evaporator is very complicated. Under the action of the complex scraper scraping, gas is easily drawn into the liquid film, forming a gas ring within the liquid film. As shown in Fig. 5(a), the black vertical line establishes four axial cross-sections in the circumferential direction. There are many gas rings in the circumferential direction, wrapping around the material. As illustrated in Fig. 5(b), sections Ⅰ−Ⅳ display the shapes of gas at different circumferential positions after entering the liquid film: the bow wave entrains gas as it moves in a spiral motion, and this gas flows out of the notch with the drag-flow; during the outflow process, some gas is entrapped between the drag-flow and the

liquid film, which is called the suspended gas ring; when the suspended gas ring makes a circumferential movement, it is subjected to the squeezing action of the drag-flow and the liquid film and the centrifugal force, forming another kind of gas ring adhering to the wall, which is called the wall-attached gas ring; when the wall-attached gas ring encounters the next bow wave, the gas ring will rupture and be expelled from the liquid film with the spiral action of the bow wave. The presence of a wall-attached gas ring will make the liquid film discontinuous and affect the heat transfer efficiency at the wall.

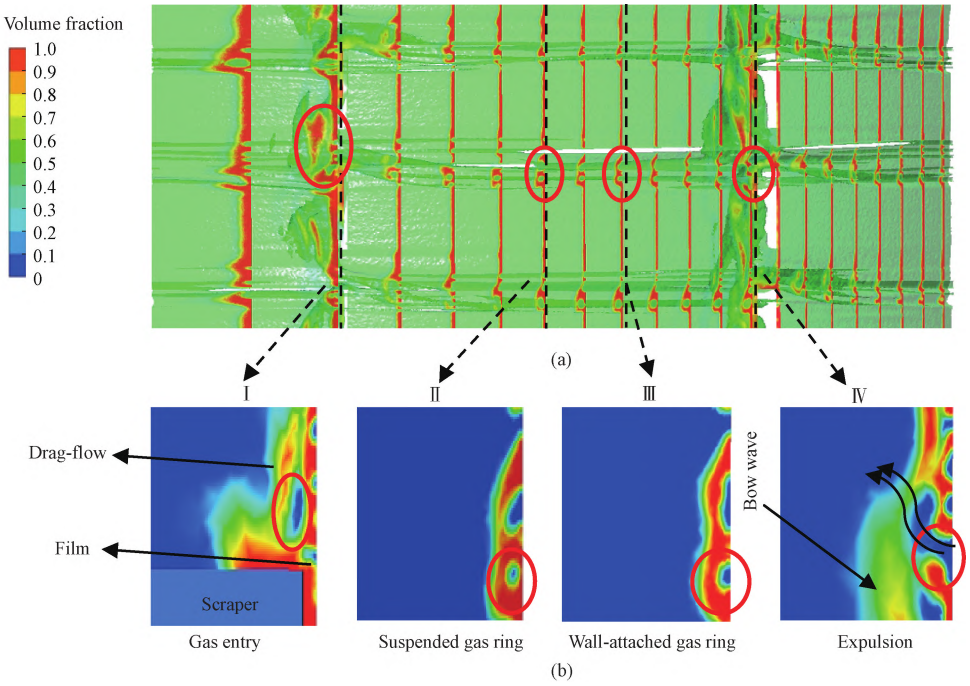

Fig. 5 Gas ring diagram in flow field: (a) flow field diagram of ATFE; (b) diagram of gas ring expulsion process

2.2.2 Gas ring generation

In the flow field, the bow wave spirals downward at the leading edge of the scraper, capturing gas as it rotates. As shown in Fig. 6(a) which illustrates how gas enters the liquid film in the ATFE, the scraper rotates counterclockwise in the left image. The blue arrow in the dashed box indicates the direction of the material flow in the field, with the material moving in the opposite direction relative to the scraper. During the movement process, the scraper will block most of the gas entrained by the bow wave, while the remaining gas will flow out with the drag-flow from the groove. As depicted in Fig. 6(a) within the black box, the blue arrows represent the gas. During circumferential motion, some gas will collide with the bow wave and change direction radially, while others will flow into the gap between the bow wave and the liquid film[23]. From Fig. 6(b), it can be observed how the gas enters the liquid film to form a suspended gas ring and how the suspended gas ring transforms into a wall-attached gas ring. Gas entrainment occurs at the gap between the bow wave and the liquid film. During the downward movement of the bow wave, some of the material will flow out of the groove, and the gas trapped between the liquid film and the bow wave will be carried out with the drag-flow. It will then be trapped in the middle of the drag-flow and the liquid film, forming a suspended gas ring. The relative speed between the drag-flow and the liquid film causes them to slowly fuse as the drag-flow moves on the liquid film. This process, combined with the squeezing action and the centrifugal force between the liquid film and the drag-flow, gradually brings the gas ring closer to the wall, forming the wall-attached gas ring.

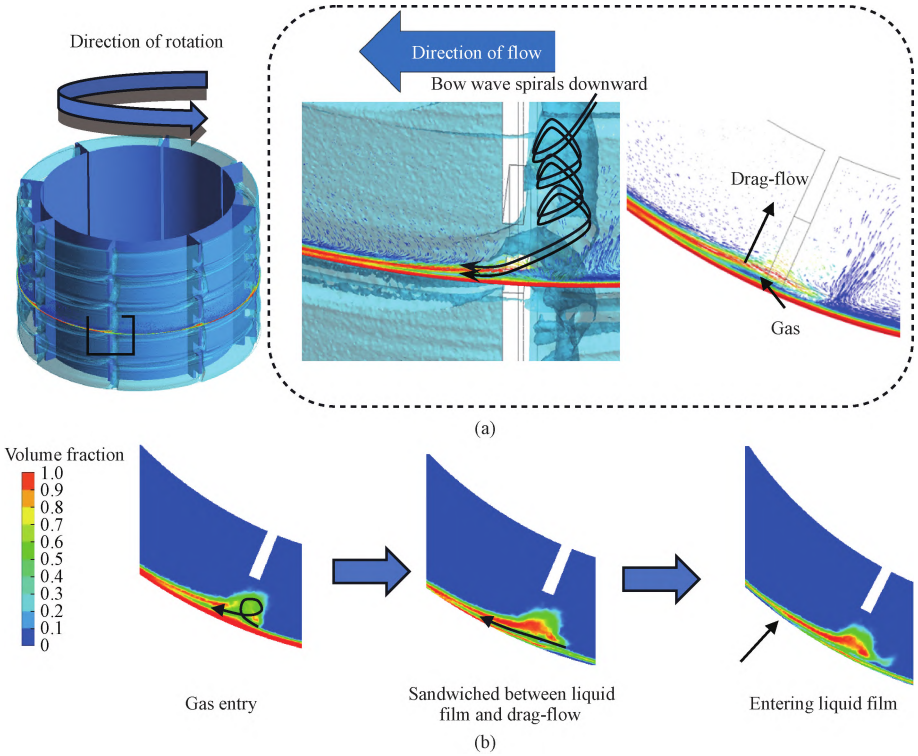

Fig. 6 Three-dimensional flow field and process of gas entering liquid film: (a) three-dimensional flow field of gas into liquid film; (b) gas entry into liquid film

2.2.3 Gas ring expulsion

In this section, the process of gas ring expulsion in the ATFE is investigated.

Figure 7 illustrates the renewal of the liquid film by a scraper, and the process of gas ring expulsion from the liquid film can be seen. Figure 7(a) intercepts a section of the bow wave in a three-dimensional flow field diagram. The fluid flows in the direction of the red arrow, and the dotted lines represent the positions of five axial sections established along the circumference, indicated by sections Ⅰ–Ⅴ. In Fig. 7(b), the gradual expulsion of the gas ring in the liquid film from section Ⅰ to section Ⅴ can be observed. Initially, with the rotation of the scraper, as shown in section Ⅰ, the gas ring sandwiched between the drag-flow and the liquid film gradually transforms into a wall-attached gas ring. Secondly, the liquid film will encounter the bow wave during the flow process, as depicted in section Ⅱ. When the drag-flow and the liquid film collide with the bow wave, as illustrated in section Ⅲ, they mix with the material in the bow wave. During extrusion and shear effects, a portion of the gas ring will be expelled along with the bow wave. The blade gap of the ATFE is only 1 mm, as depicted in sections Ⅳ and Ⅴ. Due to this narrow gap, the liquid film cannot pass smoothly between the scraper and the wall, causing it to collide with the scraper and resulting in the removal of residual gas from the solid-liquid interface. The gas ring position will be filled with material, and the liquid film will be replenished. The findings indicate that during the gas ring expulsion process, the bow wave ruptures the gas ring, while the scraper scraping promotes the renewal of the liquid film.

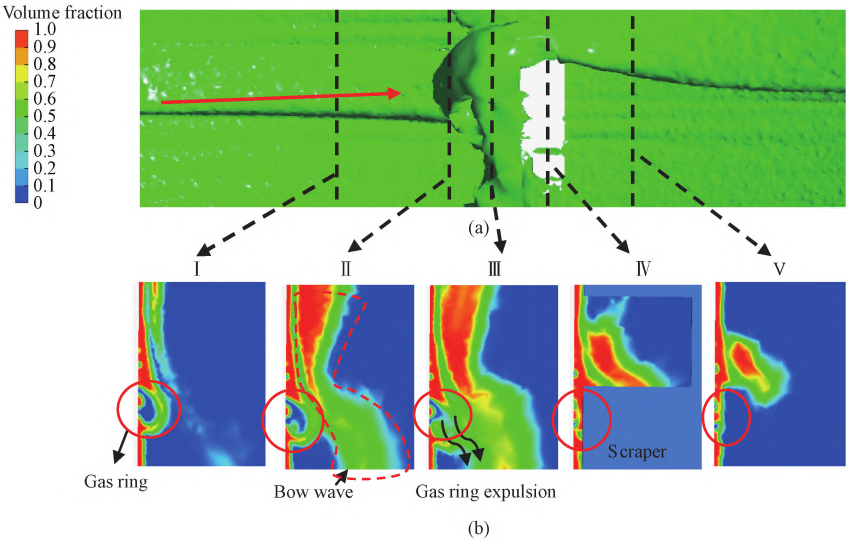

Fig. 7 Diagram of gas ring expulsion process: (a) flow field; (b) process of gas ring expulsion from liquid film

2.3 Two ways for gas ring reduction

As mentioned above, gas is trapped between the drag-flow and the liquid film when the bow wave flows out of the groove to form a drag-flow, forming a gas ring. The gas ring is expelled because the bow wave at the leading edge of the scraper plays the role of rupturing the gas ring, and at the same time, the scraping of the scraper promotes the renewal of the liquid film. This section summarizes two ways to reduce the gas ring through the mechanism of gas ring expulsion and entry.

2.3.1 Promotion of gas ring expulsion

In this section, simulations are conducted for two configurations of scrapers as illustrated in Fig. 8. The flow fields of an 8-row sawtooth scraper, an 8-row staggered scraper and a 16-row staggered scraper are compared. The blue arrows indicate the direction of the material flow. In the sawtooth scraper, the material can pass through the grooves of the two rows of scrapers. In the staggered scraper, the material will hit the scraper when passing through the grooves, allowing each area in the axial direction to be scrapped. The staggered arrangement of scrapers in multiple rows will complete the process of expelling gas rings more times in the circumferential direction.

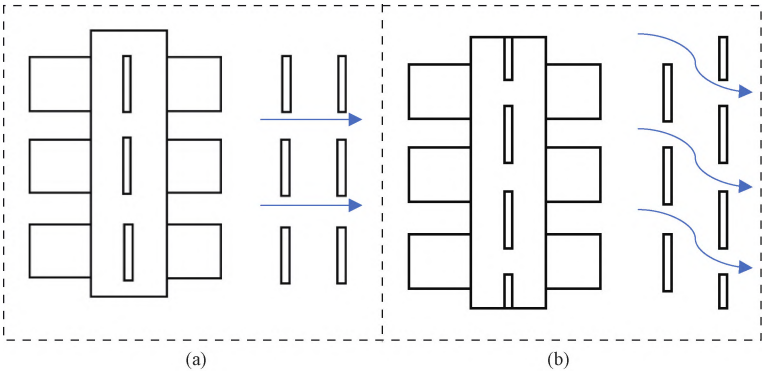

Fig. 8 Scraper arrangement: (a) sawtooth scraper; (b) staggered scraper

Figure 9 shows the distribution of the liquid film on the wall surface of various scrapers under identical working conditions. The area of liquid film formation on the wall differs for the three types of scrapers, and both the sawtooth scraper and the staggered scraper have gas rings interspersed on the wall surface. In this paper, data above 0.5 are considered to represent the liquid phase, while data below 0.5 are considered to represent the gas phase. In Fig. 9, the liquid film area ratio on the wall is defined as the ratio of the number of liquid-phase volume fraction grids on the wall to the total number of grids on the wall. The liquid film coverage on the wall is 90.8% for the 8-row sawtooth scraper, 94.9% for the 8-row staggered scraper and 96.3% for the 16-row staggered scraper. Under identical working conditions, the staggered scraper exhibits a 4.1% increase in the liquid film area on the wall compared to the sawtooth scraper. Additionally, the 16-row staggered scraper shows a 1.4% increase in the liquid film area on the wall compared to the 8-row staggered scraper. The staggered arrangement of the scrapers ensures that the process of expelling gas rings is completed at every position in the axial direction. Staggered scrapers facilitate a more thorough renewal of the liquid film on the wall, helping to expel gas rings

from the wall. Increasing the number of scraper rows can enhance the scraping frequency of the scraper. Under the same working conditions, the 16-row staggered scraper completes the process of gas ring expulsion twice as many times as the 8-row staggered scraper in the circumferential direction. Therefore, increasing the number of rows of scrapers can more effectively promote the expulsion of wall-attached gas rings. Excessive wall-attached gas rings will affect the wall heat flux of the ATFE. To enhance the evaporation efficiency of the ATFE, it is necessary to decrease the number of wall-attached gas rings in the liquid film. In contrast, the staggered scraper ensures that the liquid film spreads more uniformly on the wall, providing an advantage over the sawtooth scraper. Increasing the number of rows in the staggered scraper also helps to enhance the frequency of the gas ring expulsion process, thereby promoting more effective expulsion of wall-attached gas rings.

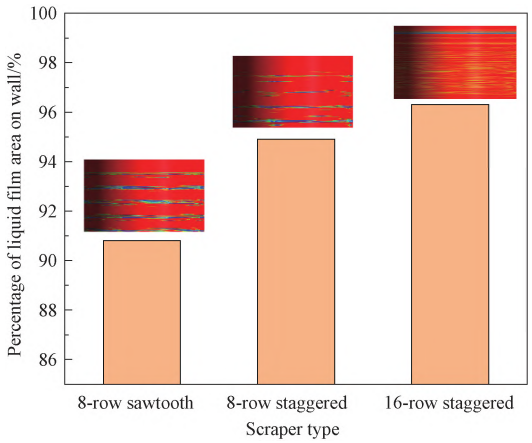

Fig. 9 Percentage of liquid film area on wall of different scrapers

2.3.2 Gas ring reduction at source

As mentioned earlier, the gas ring is formed due to the spiral effect of the bow wave. This section examines the impact of the bow wave on the gas ring. Larger bow wave sizes can easily entrain gas into the liquid film. A method is proposed to control the gas ring from the source by regulating the size of the bow wave. As shown in Fig. 10(b), the left part of the box displays the three-dimensional flow field diagram of the ATFE, while the right part shows the cross-section diagram of the bow wave. When the rotation speed increases, an obvious phenomenon is observed: the size of the bow wave gradually decreases and may even almost disappear.

Figure 11 illustrates that as the rotation speed increases, the volume percentage of the bow wave gradually decreases from 65% to 13%. The gas ring in the liquid film decreases as the rotation speed increases due to the spiral action of the bow wave which is the primary cause of the gas ring. When the rotation speed increases, the scraper compresses the bow wave into the liquid film, causing the specific gravity of the bow wave to decrease within the evaporator material.

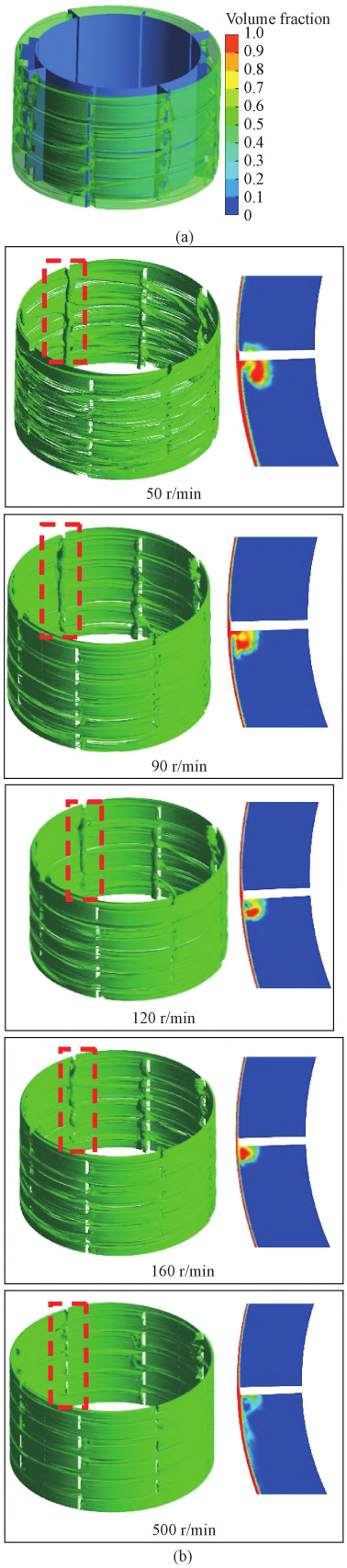

Fig. 10 Three-dimensional flow field diagrams: (a) liquid film in flow field; (b) size of bow wave at different rotation speeds

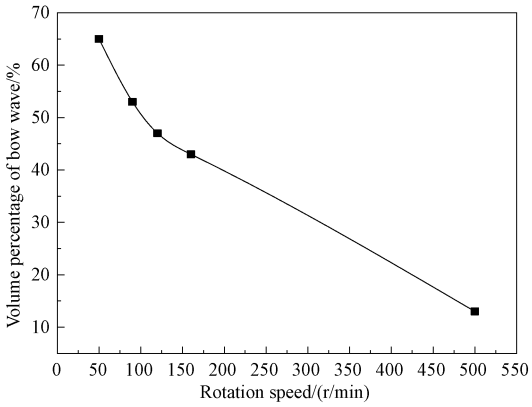

Fig. 11 Volume percentage of bow wave at different rotation speeds

A decrease in the size of the bow wave will also lead to a decrease in the gas ring. As depicted in Fig. 12, the cross-sections of the drag-flow at various rotation speeds are illustrated, with the blue area in the middle representing the gas ring sandwiched between the drag-flow and the liquid film. As the rotation speed increases, the gas ring in the liquid film undergoes a gradual change. At 50 r/min, the gas ring is visible throughout the wall. As the rotation speed increases to 90 r/min, the drag-flow gradually decreases, and the gas ring sandwiched between the drag-flow and the liquid film diminishes. When the rotation speed reaches 500 r/min, the size of the bow wave becomes significantly smaller, and the drag-flow from the groove almost disappears. At this point, the gas cannot be sandwiched between the drag-flow and the liquid film. The gas ring loses its way to enter the liquid film, and the gas ring in the liquid film almost disappears. As previously mentioned, the size of the bow wave in the ATFE flow field is critical for generating the gas ring, and reducing the size of the bow wave can decrease the gas ring.

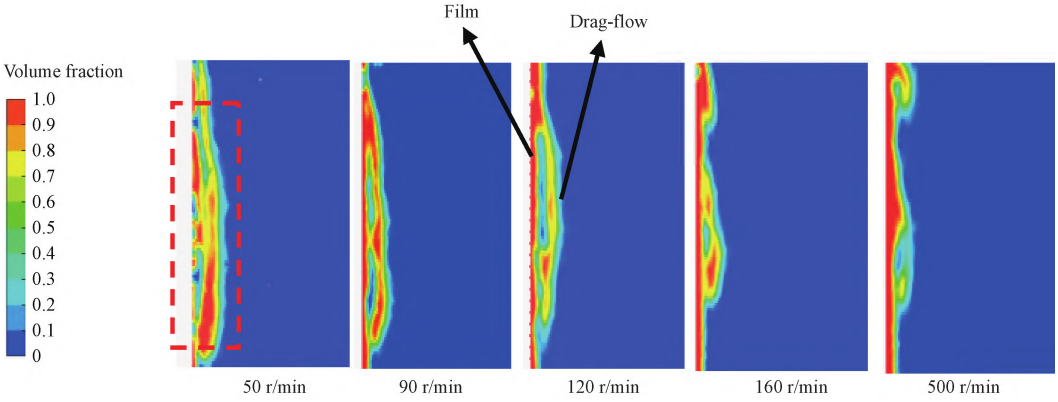

Fig. 12 Phase diagram of gas ring inside liquid film at different rotation speeds

The gas entering the liquid film decreases, causing the wall-attached gas ring to shrink, which leads to a higher percentage of the wall covered by the liquid film. As depicted in Fig. 13, the phase diagram illustrates the film formation on the wall at various rotation speeds of the staggered scraper. When the scraper speed is 50 r/min, an obvious gas ring forms on the wall surface. However, as the speed gradually increases from 50 r/min to 500 r/min, the size of the bow wave decreases, the drag-flow from the groove reduces, and the gas ring near the wall surface gradually diminishes. The curve shown in Fig. 13 depicts the variation of the percentage of the liquid film area on the wall with the rotation speed. Firstly, as the rotation speed increases from 50 r/min to 500 r/min, the percentage of the liquid film area on the wall increases from 84.4% to 96.2%. Additionally, the liquid film spreading on the wall becomes more homogeneous, aligning with the phase diagram of the liquid film on the wall. However, the gas in the liquid film will not completely dissipate. Su[24] found that the probability of bubble breakage increased with the increase in the rotation speed when studying the breakage of bubbles in the stirring device. The probability of bubble breakage slows down as the rotation speed increases due to the instability of the turbulent flow field, ultimately stabilizing at around 97.0%. It can also be observed in Fig. 13 that at 500 r/min, the percentage of the liquid film area on the wall increases gradually to approximately 96.2%, consistent with the experimental data from Su[24].

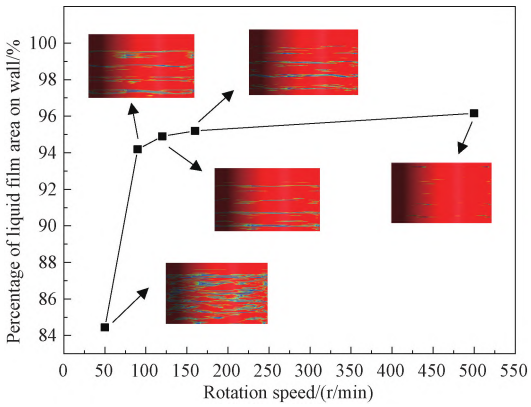

Fig. 13 Percentage of liquid film area on wall

The helical action of the bow wave is the source of the gas ring in the liquid film, and the reduction of the bow wave can suppress the formation of the gas ring. As shown in Fig. 14, the bow wave is getting smaller according to the viscosity phase diagram. The material at the tip of the scraper is sheared by the scraper, the shear-thinning effect is obvious, and the viscosity is the lowest. The viscosity of the circled wave at the leading edge of the scraper is higher than that at the scraper tip. The higher the rotation speed, the smaller the viscosity and the size of the circled wave. As shown in Fig. 15, the positions of the scrapers are at 30° and 60°, respectively. The data are extracted at the same location as in Fig. 4. As the rotation speed increases, the shearing effect of the scraper on the material increases and the viscosity of the material in the ATFE gradually decreases. In the interval of 30° and 60°, the average viscosity is about 2.0 Pa · s at 50 r/min, and the average viscosity decreases to 0.5 Pa · s at 500 r/min. In the position of the scraper tip, the viscosity gradually decreases when the rotation speed grows from 50 r/min to 120 r/min, and when the rotation speed is higher than 120 r/min, the viscosity at the position of the scraper tip almost no longer decreases, and is roughly around 0.2 Pa · s. A closer look reveals an interesting phenomenon: as the speed increases, the difference between the viscosity at the scraper and the viscosity at the liquid film gradually decreases. At 500 r/min, the viscosity at the bow wave position is almost the same as that of the liquid film.

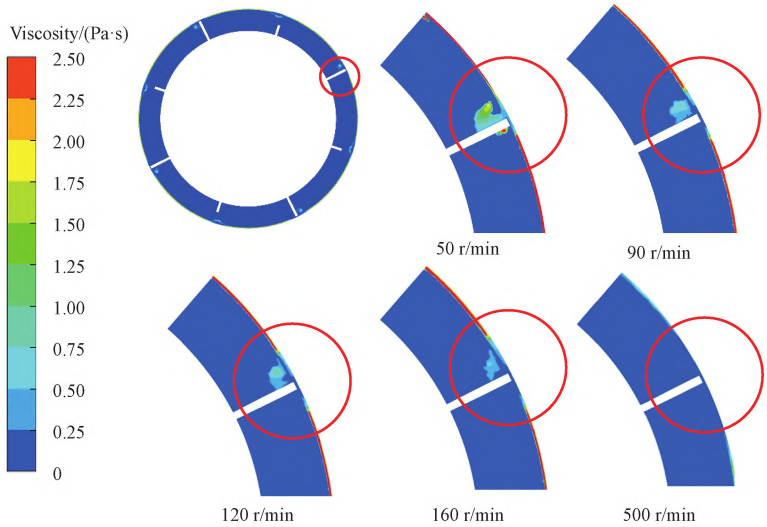

Fig. 14 Phase diagram of liquid film viscosity

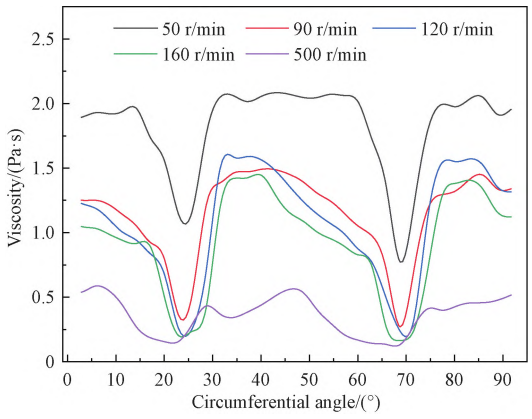

Fig. 15 Viscosity in circumferential direction of ATFE

3 Conclusions

The gas ring in the flow field of the ATFE under various scraper configurations and rotation velocities was examined. The findings are summarized as follows.

1) The spiral motion of the bow wave is crucial for inducing the gas to enter the liquid film. In the flow field, the material in the bow wave flows out of the groove in the middle of the scraper, creating a drag-flow and carrying the gas into the liquid film. Reducing the size of the bow wave can decrease the generation of gas rings from the source. This can be achieved by increasing the rotation speed.

2) During the gas ring expulsion process, the gas ring initially encounters the bow wave, leading to rupture and expulsion. Subsequently, the liquid film can be renewed through the scraping action of the scraper. Effective promotion of gas ring expulsion can be achieved by altering the scraper arrangement and increasing the number of scraper rows.

3) When choosing the scraper arrangement in the ATFE, the staggered type of the scraper is prior to ensure a more uniform spreading of the liquid film on the wall surface, and the number of scraper rows should increase as needed. In addition, decreasing the size of the bow wave can minimize the wall surface gas ring. Increasing the rotation speed can also help reduce the size of the bow

wave. However, it is not possible to infinitely reduce the size of the bow wave to minimize the gas ring, because the bow wave facilitates the exchange of substances when it vigorously mixes with the liquid film, and there is a limit value to the percentage of the liquid film area on the wall. The minimum rotation speed should ensure that the shear thinning at the scraper is close to the maximum value, while the maximum rotation speed should ensure that the liquid film spreads uniformly on the wall without the bow wave disappearing.

References

[1] JASCH K, GRÜTZNER T, ROSENTHAL G, et al. Experimental investigation of the residence time behavior of a wiped film evaporator[J]. *Chemical Engineering Research and Design*, 2021, 165: 162-171.

[2] PI P H, YANG Z R, MA S P. Advantages and applications of wiped thin-film evaporators[J]. *Modern Chemical Industry*, 2001, 21(3): 41-44. (in Chinese)

[3] MUTZENBURG A B. Agitated thin film evaporators[J]. *Chemical Engineering*, 1965, 9: 175-190.

[4] MCKELVEY J M, SHARPS G V Jr. Fluid transport in thin film polymer processors[J]. *Polymer Engineering & Science*, 1979, 19(9): 651-659.

[5] KOMORI S, TAKATA K, MURAKAMI Y. Flow structure and mixing mechanism in an agitated thin-film evaporator[J]. *Journal of Chemical Engineering of Japan*, 1988, 21(6): 639-644.

[6] KERN D Q, KARAKAS H J. Mechanically aided heat transfer[J]. *Chemical Engineering Progress*, 1959, 55(29): 4175468.

[7] KOOL J. Heat transfer in scraped vessels and pipes handling viscous materials[J]. *Transactions of the Institution of Chemical Engineers*, 1958, 36: 253-258.

[8] ABDOULAYE C, LING X P, BI J L, et al. Effect of bubble coalescence on the wall heat transfer during subcooled pool boiling[J]. *Journal of Tsinghua University (Science and Technology)*, 2014, 54(2): 240-246.

[9] WEI J H, PAN L M, CHEN D Q, et al. Numerical simulation of bubble behaviors in subcooled flow boiling under swing motion[J]. *Nuclear Engineering and Design*, 2011, 241(8): 2898-2908.

[10] FAN X C, ZHANG L, BO S, et al. Boiling and evaporation of liquid films and phase interface fluctuation in vertical down tubes[J]. *Acta Energiae Solaris Sinica*, 2019, 40(8): 2258-2265. (in Chinese)

[11] HAO Q, LI J C, GENG D Q. Research on bubble behavior and heat transfer characteristics of flow boiling in rifled tubes[J]. *Cryogenics & Superconductivity*, 2020, 48(5): 59-65. (in Chinese)

[12] ZHENG S S. Research on numerical simulation of flow characteristics and optimal design for agitated thin film evaporator[D]. Shanghai: Donghua University, 2022. (in Chinese)

[13] HANN D B, CHERDANTSEV A V, AZZOPARDI B J. Study of bubbles entrapped into a gas-sheared liquid film[J]. *International Journal of Multiphase Flow*, 2018, 108: 181-201.

[14] ZENIT R, FENG J J. Hydrodynamic interactions among bubbles, drops, and particles in non-Newtonian liquids[J]. *Annual Review of Fluid Mechanics*, 2018, 50: 505-534.

[15] OHTA M, IWASAKI E, OBATA E, et al. A numerical study of the motion of a spherical drop rising in shear-thinning fluid systems[J]. *Journal of Non-Newtonian Fluid Mechanics*, 2003, 116(1): 95-111.

[16] CHEN X, PENG Y T, HUANG Y, et al. Numerical simulation of flow field and flow state division in thin-film evaporators[J]. *Journal of Donghua University (English Edition)*, 2024, 41(5): 525-535.

[17] YANG Y F, WANG J L, WANG J Z, et al. Pore-scale numerical simulation of supercritical CO_2-brine two-phase flow based on VOF method[J]. *Natural Gas Industry*, 2023, 43(3): 69-77. (in Chinese)

[18] SHAMS M, RAEINI A Q, BLUNT M J, et al. A numerical model of two-phase flow at the micro-scale using the volume-of-fluid method[J]. *Journal of Computational Physics*, 2018, 357: 159-182.

[19] ZENG Y, WANG H B, SUN M B, et al. SST turbulence model improvements: review[J]. *Acta Aeronautica et Astronautica Sinica*, 2023, 44(9): 103-134.

[20] GHANNAM M T, ESMAIL M N. Rheological properties of carboxymethyl cellulose[J]. *Journal of Applied Polymer Science*, 1997, 64(2): 289-301.

[21] OSTWALD W. de Waele-Ostwald equation[J]. *Kolloid Zeitschrift*, 1929, 47(2): 176-187.

[22] ZHENG S S, HUANG Y, ZOU K, et al. Numerical simulation of flow pattern for non-Newtonian flow in agitated thin film evaporator[J]. *Acta Physica Sinica*, 2022(5): 71. (in Chinese)

[23] WANG Z W, CHENG R L, HUANG Y, et al. Numerical simulation of flow field distribution and transmission characteristics in thin film evaporator[J]. *Journal of Donghua University (Natural Science)*, 2023, 49(2): 77-84. (in Chinese)

[24] SU B Q. Study of single bubble breakup in stirred tank [D]. Beijing: Beijing University of Chemical Technology, 2019. (in Chinese)

刮膜式薄膜蒸发器内液膜中气环的生成及排出

柴 进, 黄 瑶*, 彭倚天, 邹 鲲
东华大学 机械工程学院, 上海 201620

摘 要: 刮膜式薄膜蒸发器是应用于蒸发浓缩的关键设备, 处理高黏度非牛顿流体的刮板结构十分复杂。在复杂刮板的刮擦下, 气体会进入液膜并形成壁面气环, 进而降低壁面热流并影响传热。该文基于计算流体力学模拟了薄膜蒸发器中非牛顿流体的流场, 探讨了液膜中壁面气环生成的机理并提出了抑制壁面气环生成的方法。研究结果表明, 气体在进入液膜后先转变成膜内气环, 再演变成壁面气环。刮板对液膜的周向刮擦能够促进气环排出, 因此调整刮板的排列方式并提高刮板的刮擦频次可以促进气环排出。圈形波的螺旋作用是气体进入液膜的源头, 减小圈形波的尺寸能够有效抑制气体进入液膜, 可以通过提高薄膜蒸发器转子转速来减小圈形波的尺寸, 从源头减少气环的生成。该文针对气环的生成和排出进行研究, 进一步为薄膜蒸发器处理非牛顿流体的研究提供理论指导。

关键词: 刮膜式薄膜蒸发器; 非牛顿流体; 气环; 高黏度